Microthermography of diode lasers: The impact of light propagation on image formation

Julien LeClech, Mathias Ziegler, Jayanta Mukherjee, Jens W. Tomm', Thomas Elsaesser, Jean-Pierre Landesman, Brian Corbett, John G. McInerney, Johann Peter Reithmaier, Stefan Deubert, Alfred Forchel, Włodzimierz Nakwaski, and Robert P. Sarzała

Citation: Journal of Applied Physics **105**, 014502 (2009); doi: 10.1063/1.3055356
View online: http://dx.doi.org/10.1063/1.3055356
View Table of Contents: http://aip.scitation.org/toc/jap/105/1
Published by the American Institute of Physics

Microthermography of diode lasers: The impact of light propagation on image formation

Julien LeClech,[1,2] Mathias Ziegler,[1] Jayanta Mukherjee,[3] Jens W. Tomm,[1,a)] Thomas Elsaesser,[1] Jean-Pierre Landesman,[2] Brian Corbett,[3] John G. McInerney,[3] Johann Peter Reithmaier,[4] Stefan Deubert,[5] Alfred Forchel,[5] Włodzimierz Nakwaski,[6] and Robert P. Sarzała[6]

[1]*Max-Born-Institut, Max-Born-Str. 2 A, 12489 Berlin, Germany*
[2]*Faculté des Sciences et Techniques de l'Université de Nantes, 2, Rue de la Houssinière, BP 92208, 44322 Nantes Cedex 3, France and Polytech' Nantes, La Chantrerie, Rue Christian Pauc, BP 50609, 44306 Nantes Cedex 3, France*
[3]*Department of Physics and Tyndall Institute, National University of Ireland, University College, Cork, Ireland*
[4]*Institute of Nanostructure Technologies and Analytics, Technische Physik, Universität Kassel, Heinrich-Plett-Str. 40, 34132 Kassel, Germany*
[5]*Technische Physik, Universität Würzburg, Am Hubland, 97078 Würzburg, Germany*
[6]*Laboratory of Computer Physics, Institute of Physics, Technical University of Łódź, ul. Wólczańska 219, 93-005 Łódź, Poland*

(Received 15 September 2008; accepted 12 November 2008; published online 6 January 2009)

We analyze the effect of propagating infrared thermal radiation within a diode laser on its thermal image taken by a thermocamera. A ray-tracing analysis shows that this effect substantially influences image formation on a spatial scale of 10 μm, i.e., in the domain of microthermography. The main parameter affecting the thermal radiation spread in the semitransparent semiconductor structure is the free carrier concentration in the substrate, governing its absorption. Two applications are presented: a quantum dot laser and a quantum-well laser, where independent thermal models are developed using the finite element method (FEM). Our ray-tracing analysis verifies the FEM simulated temperature profiles by interlinking them to experimental temperature maps obtained through microthermography. This represents a versatile experimental method for extracting reliable bulk-temperature data from diode lasers on a microscopic scale. © *2009 American Institute of Physics*. [DOI: 10.1063/1.3055356]

I. INTRODUCTION

Recent technological progress in the field of infrared (IR) thermography has paved the way for many novel applications, among others thermographic analysis of optoelectronic devices. Imaging thermography has already been applied to inspection of diode lasers, light-emitting diodes,[1] and even to two-dimensional (2D) stacked high-power diode laser arrays.[2] The spatial resolution has reached values <10 μm for a system operating at wavelengths in the first atmospheric window.[3] This capability provides an option to probe *thermal profiles* across various optoelectronic devices that have typical dimensions of several hundred microns. This is a completely new approach because so far only time-consuming scanning techniques such as micro-Raman spectroscopy provided similar results for the surfaces of such devices.[4] Thermography relies on the measurement of thermal radiation. As long as opaque materials with known and high enough emissivity are probed, careful calibration can help us extract very useful results. The situation, however, becomes more difficult for semitransparent semiconductor materials, as is the case of GaAs-based optoelectronic devices. There, the spread of propagating thermal IR light is expected to alter the original thermal image of the semiconductor parts of optoelectronic devices at least on a microscopic scale on the order of 10–50 μm. In addition, internal reflections at the metallic contacts, e.g., of diode lasers, result in a cavity enhancement of the thermal radiation as analyzed for extended devices and test samples in Ref. 5.

The basic goal of our present study is to quantify propagation effects, thereby qualifying *microthermography* (MT) as a practical tool that allows verification of thermal profiles from model predictions based on, e.g., FEM. Our approach is organized in the following way. We model the spreading of propagating IR radiation inside the laser diode using a ray-tracing technique. As input for this modeling, knowledge of the original thermal distribution in the device volume is required. Since there is no alternative experimental tool yet to access such distributions, we use results from thermal FEM modeling. After converting the bulk-temperature distribution into a distribution of IR light sources, the propagation of thermal radiation is modeled by ray tracing. The impact of material parameters such as absorption coefficient α, refractive index n, and reflectivity R will be discussed. Finally, we apply ray-tracing modeling to the FEM results for two particular device designs and compare the results with experimental data obtained from measurements with a thermocamera. For this comparison we have chosen two different types of devices. The first example involves thermal profiling of a quantum dot (QD) laser. This is of particular interest because

a)Electronic mail: tomm@mbi-berlin.de.

the standard method for thermal characterization of diode lasers, namely, the use of thermally induced emission wavelength shift, widely fails for QD devices. In the second example we analyze time-dependent thermal images from a quantum-well (QW) device during pulsed operation. In this case we take benefit from the fact that IR light spreads much faster than any time constant, describing the thermal turn-on dynamics in such a device. Both examples demonstrate the applicability of our approach and provide a general guideline for further usage of the MT technique.

II. EXPERIMENTAL

A. Analyzed devices

The 950 nm emitting broad-area (BA) QD lasers are based on a large optical spot size design with a 2.5 μm thick $Al_{0.3}Ga_{0.7}As$ core region. Three layers of highly strained $In_{0.53}Ga_{0.47}As$ QDs are spaced within 30 nm of GaAs spacer layers. The structure is grown by molecular beam epitaxy on GaAs substrates. Photoluminescence measurement shows wavelengths of 934 and 901 nm for the fundamental and the next higher interband transitions, respectively. 50 μm wide silicon dioxide isolated stripe lasers were fabricated using TiPtAu as the *p*-side contact metallization. Samples were thinned to approximately 100 μm and AuGeNi metallization was used as the *n* contact. Devices of various lengths were characterized. The device under consideration has its contact stripe asymmetrically placed on the 500 μm wide device. The stripe center is located at 185 μm from one side. The 1.5 mm long *p*-side down packaged device had a threshold current of 0.45 A, with total slope efficiency of 0.72 W/A, and lasing wavelength at 950 nm. While a total of four devices were analyzed, we confine the presentation here to one device.

High-power BA QW lasers emitting at 808 nm were grown by metal-organic vapor phase epitaxy on GaAs substrates. A tensile strained GaAsP QW serves as the gain medium. The chip dimensions are $1500\times500\times115$ μm^3 (length $\times$ width $\times$ height) and the width of the active stripe is 130 μm; see Fig. 1(a). Standard cleaning, passivation, and coating processes were applied to both the front and rear facets. The devices are hard-soldered *p*-side down onto 300 μm thick CuW heat spreaders, which are attached to C mounts on a temperature stabilized heat sink. The lasing threshold is 0.6 A and the output power at 5 A of operating current was about 4 W. More details on these structures are given in Ref. 6 and Ref. 7 presents some preliminary MT results and qualitative assignments. Two devices have been measured but for clarity the analysis is focused here to one of them only.

B. Microthermography

Thermographic measurements were performed with a 384×288 pixel Thermosesorik CMT 384M camera microscope with a detection range confined to the 3.5–6.0 μm wavelength window and diffraction limited to a spatial resolution of about 6 μm. A temperature calibration was made by taking images of the nonoperating device between 25 and 35 °C in steps of 2 K. The corresponding temperature versus

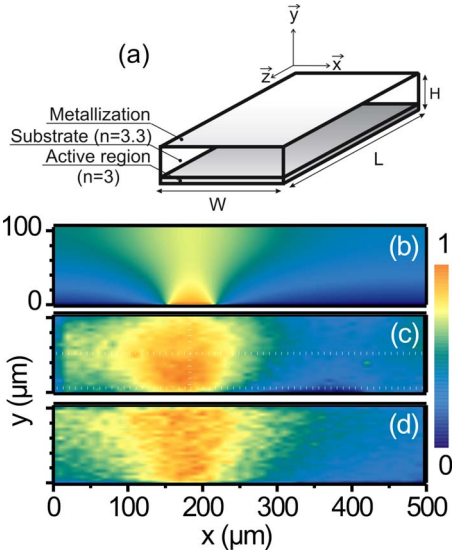

FIG. 1. (Color online) (a) Schematic of the laser device showing its principal parts, namely, the active region, the substrate, the top and bottom metallizations (only the top is shown), and the coordinate system used in the text. The front facet that is probed in the experiment lies in the *x*-*y* plane facing the observer. (b) Temperature distribution in the *x*-*y* plane of a QD laser resulting from a 2D-FEM calculation. (c) MT image from the front facet of a QD laser operated at 1.8 A. (d) Thermal emission distribution detected in front of the laser front facet as modeled with ray tracing of the temperature distribution shown in (b). The dotted white lines represent the positions of cuts which will be shown in Fig. 4.

camera signal curve is perfectly described by a third order polynomial. Temperature-calibrated images obtained in this way are presented for the QD laser in Fig. 1(c).

For monitoring thermal properties in pulsed operation, we apply a time-dependent synchronous undersampling lock-in thermography technique.[7] This allows, via variation of the electrical pulse width, recording of quite different transient thermal situations with high signal-to-noise ratios. Short pulses with durations on the order of 100 μs create a narrow temperature distribution with only limited heat spreading away from the emitter stripe, whereas long pulses on the order of 10–100 ms almost resemble a steady-state situation with the heat spreading across the entire device. In the time-resolved lock-in measurement thousand heating and cooling cycles of the laser diode are sampled. Four frames per period are successively correlated with a rectangular correlation function, leading to a single image with a temperature distribution characteristic for that transient situation. With model data for times between 0.2 μs and 100 ms, the correlation is simulated by summing the product of the thermal model data for the active region center and the correlation function over a single pulse. Comparison of the resulting temperature with the modeled temperature transient determines the point in time where both agree. Times calculated in this way are smaller than the used pulse width inasmuch as the temperature transient deviates from the rectangular shape of the correlation function. In good approximation those transients are characterized by a few exponential time constants.[8] For analysis we use data sets that correspond to times of 15 μs and 11 ms after turn-on of the laser diode.

III. MODELING

A. Thermal FEM modeling

For the QD laser we apply a 2D steady-state electrothermal FEM (Ref. 9) model because effects related to heat spreading along the laser axis such as facet heating are not considered. The temperature profile and current spreading in the device were simulated using the model developed in our earlier work.[10] No current spreading was assumed in the substrate on account of the high mobility of electrons. In addition to Joule heating, distributed heat sources taken into account in the model include reabsorption of stimulated and spontaneous emission as well as nonradiative recombination.[10] Epistructure-dependent radiative transfer heating[10] is not involved and hence not considered in the model. Heat transfer via convection and radiation was also not included in the final model as it was found to be of little effect. The 2D heat-conduction equation coupled with Laplace's equation was self-consistently solved in the steady state using FEM in a 2D lateral cross section. A fluxless Neumann boundary (thermal insulation) is assumed at all the laser air interfaces and a Dirichlet boundary is assumed at the In-solder Cu-heat sink interface. The Dirichlet boundary (equal to ambient temperature) assumes that the Cu-heat sink is of infinite thermal conductivity. We believe that this usual assumption[11] might affect the actual magnitude of the temperature but not its lateral profile. Both asymmetric and symmetric devices were simulated to quantify the effect of asymmetry on temperature profile. Figure 1(b) shows the temperature distribution as calculated for the device and the temperature distribution under operating conditions is shown in Fig. 1(c).

The thermal cross sections of the QW laser are obtained from transient 2D-FEM simulation. For the heat sources we took into account the active-area heating by nonradiative recombination, absorption of radiation within this area, absorption of energy transferred radiatively from the active area, generation of heat via Ohmic losses at the contacts, and Joule heating.[12,13] The heat-generation rate of the active region is extracted from experimental current-voltage and current-output power characteristics. The bottom surface of the C mount linked to the Peltier cooler is assumed to be fixed at the ambient temperature, whereas the other surfaces of the structure are considered to be thermally isolated. Temperature-dependent thermal conductivities of all materials are taken into account.[14] The heat-conduction equation is solved using the variational formulation of FEM based on the Euler theorem.[9] The time step is steadily increased from 0.1 to 150 ms.

B. Ray-tracing modeling

The ray-tracing model was implemented using commercially available ZEMAX® software.[15] The device geometry depicted in Fig. 1(a) is represented by two rectangular parallelepipeds, one for the substrate and the other for the epitaxial structure with the active region in the center. The substrate consists of GaAs, and the epitaxial structure is averaged over its different semiconductor layers since each of them has a thickness smaller than the wavelength of the relevant thermal radiation (5 μm). Typically 10^7–10^8 monochromatic rays with random polarization start from random points inside the diode laser in random directions until they reach a detector array or until they are damped to 0.1% of their initial power. The light sources correspond to results from FEM calculations. The calculated temperature distributions are transformed into distributions of thermal IR light sources after application of the experimental thermocamera calibration curve; see Sec. II B. Such a calibration links the thermal emission power of the laser device as seen by the thermocamera to the corresponding temperature, without getting into determination of emittance of its semiconductor materials, which turns out to be quite involved.[5] Ray-tracing applies geometrical optics and material absorption to predict the trajectory and power of the light rays inside a linear medium. Without losing generality, monochromatic light of a wavelength of 5 μm is used according to a weighted average over the detection range of our thermocamera system.

With these approximations, our ray-tracing approach takes into account the following parameters: the refractive index n, the absorption coefficient α of the semiconductor material sections at a wavelength of 5 μm, and the (specular) reflectance of the opaque metallic contact surfaces R. To a good approximation, α can be assumed to be identical in the substrate and the epilayer section. R is assumed identical for both top and bottom metallizations. From microreflectivity measurements the effect of the front and reverse facet dielectric coatings has been found to be negligible within the relevant IR spectral range as compared to uncoated surfaces.

The detector in the simulations is placed outside the laser device close to its front facet detecting the residual power from individual rays. Spatial resolution of the sources and the detector array in the x-y plane [see Fig. 1(a)] is chosen to 58×14 pixels in the case of QW laser and 28×14 pixels in the case of the QD laser, and the experimental data is averaged accordingly.

IV. RESULTS AND DISCUSSION

A. The impact of thermal infrared light propagation on the shape of thermographic images

The discrepancy between results from FEM calculation [Fig. 1(b)] that is tentatively assumed to represent the "true" thermal distribution and the MT image [Fig. 1(c)] clearly shows that a major broadening mechanism is manifested in the experimental maps. The intrinsic blurring according to the point-spread function of the high-magnification MT system in the diffraction limited regime might explain to some degree the disagreement between absolute temperatures around the active region which contains large temperature gradients. The additional substantial broadening reaching far into the substrate, however, cannot be explained in this way. In the following we show how spreading of thermal radiation on a microscopic scale is responsible for a broadened shape of the MT images obtained from semitransparent semiconductor diode lasers.

We start with a FEM-modeled temperature distribution of the QW-laser structure; see solid black line in Fig. 2(a).[16] For ray tracing, the IR light sources are defined accordingly.

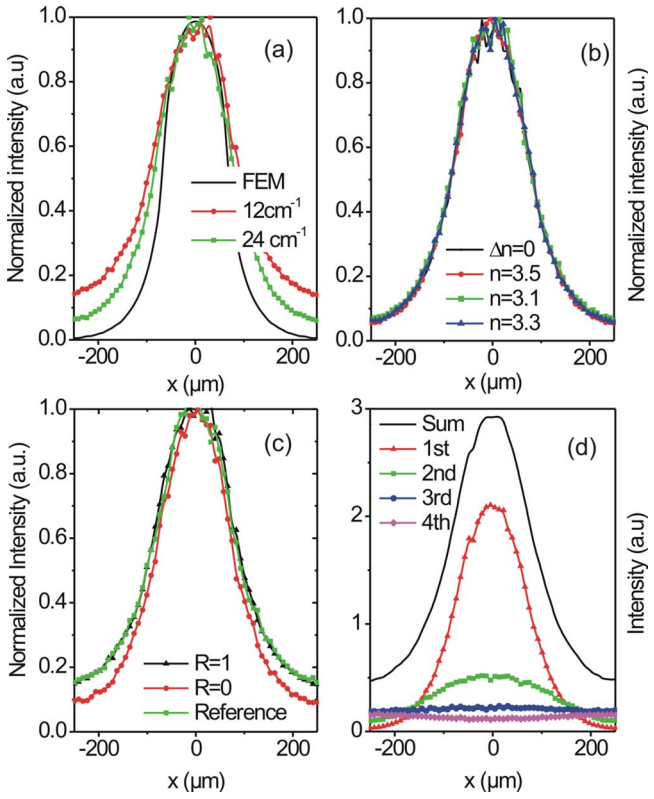

FIG. 2. (Color online) Profiles of thermal intensity distribution at active region as obtained by ray-tracing simulations of MT images for the QW laser under variation of the free parameters. (a) FEM input profile and normalized profiles for $\alpha=12$ and 24 cm^{-1}. (b) Normalized profiles for refractive-index n variation of the substrate as given in the legend. The full black line shows the result after neglecting the index step between substrate and active region. (c) Intensity profiles for a reflectivity R of the top and bottom metallizations of 1 (perfectly reflecting) and 0 (fully absorbing) and as "reference" without metallization, i.e., bare semiconductor-air interface. (d) Intensity profiles as obtained from individual ray-tracing simulations with source distributions placed in the first, second, and until fourth quarters of the device. The full black line describes the sum of these which perfectly agrees with a reference simulation of the full cavity.

Figures 2(a)–2(c) show how light propagation inside the semiconductor materials broadens the thermal image and how the determining parameters affect its actual shape. In Ref. 5 we determined $\alpha\sim 18$ cm^{-1} for a typical laser structure with a n-type substrate doping of $\sim 1.2\times 10^{18}$ cm^{-3}. In Fig. 2(a) a reasonable spread of α between 12 and 24 cm^{-1} is assumed corresponding to free electron concentrations between 0.8×10^{18} and 1.6×10^{18} cm^{-3}. Obviously, an increase in the absorption coefficient makes the image narrower and reduces the total intensity of thermal radiation escaping the device (here the scaling factor amounts to 1.3). On the other hand, the impact of a variation of the refractive index is negligible [Fig. 2(b)], even in the conservatively large chosen variation range between 3.5 and 3.1. These data correspond to the n values of GaAs at 1 and 20 μm, respectively.[17] Also the index step between the substrate and epilayer section is found to give no noticeable effect (see full black line) because in case of realistically distributed temperatures such as studied here, the thermal radiation from the thick substrate (~30 times thicker than the epilayers) dominates. The reflectivity R of the top and bottom metallic contacts determines the IR light propagation as well. A decrease in R affects the profile in Fig. 2(c) in a similar way as the increase in α in Fig. 2(a). Note that R is varied between the extreme values of 1 and 0, i.e., between totally reflecting and totally absorbing.

A phenomenological explanation for α-related broadening is given in Fig. 2(d). There ray tracing is performed analogous to Fig. 2(a) for $\alpha=12$ cm^{-1} but with distributed sources having a length of one-fourth of the total cavity length only. In particular, sources are placed at the first, then the second, and until the fourth quarter inside the cavity and the respective profiles together with the total sum are presented in Fig. 2(d). Clearly, the shape of the sum profile is most influenced by light from the first quarter, whereas the following sections, in particular, the second half of the cavity, only add a flat background contribution to the overall image. Now, an increase in α would change the relative contributions from different cavity depths in favor of the regions closest to the front facet.

Results obtained using a 2D ray-tracing model of the x-z plane along the cavity and considering sources exclusively placed at the bottom (i.e., at the active region) explain these observations; see Fig. 3. For a refractive index of 3.3 in both the active region and the epilayers, total internal reflection limits the exit angle of a point source inside the cavity to about 17.6° (with z axis). Accordingly, every 352 μm along the cavity length another reflection becomes possible, adding up to four reflections for rays coming from deeper than 1408 μm. In Fig. 3(b), IR light intensity outside the front facet is plotted versus the source position along the cavity, separately for the different components that experienced zero to four reflections, for the 112 μm high[18] and 1500 μm long cavity. Both the exponential damping with α equal to 12 and 24 cm^{-1} and the attenuation due to the index jump from 3.3 to 1 when leaving the front facet are taken into account. To be more realistic and give sense to the result displayed in Fig. 3, at each point an average over the entire allowed exit angle range is given and normalized to the maximal opening angle of ~17.6°, thereby taking variation of the path length adequately into account.

From these calculations we conclude that direct light coming through a small angle mainly from the first few hundreds of microns of the cavity length is responsible for the shape of the intensity distribution of thermal radiation that we detect from the front facet, whereas the information we get from further inside the cavity is mostly composed of up to four times reflected light, giving rise to an additional rather flat background. The total intensity versus longitudinal source position is perfectly described by a simple exponential decay with α as the decay constant. This is a consequence of the small angular range of rays escaping from the front facet, which results in an almost constant transmission coefficient at the semiconductor-air interface. It follows that an increase in α [Fig. 2(a)] or a decrease in R [Fig. 2(c)] will increase the relative amount of direct light detected outside the front facet. Interestingly, even if no metallic coating is assumed on the top and bottom surfaces, all rays that are allowed to exit the front facet experience total internal reflection at the top and bottom interfaces. Thus assuming $R=1$ is a rather fair approximation.

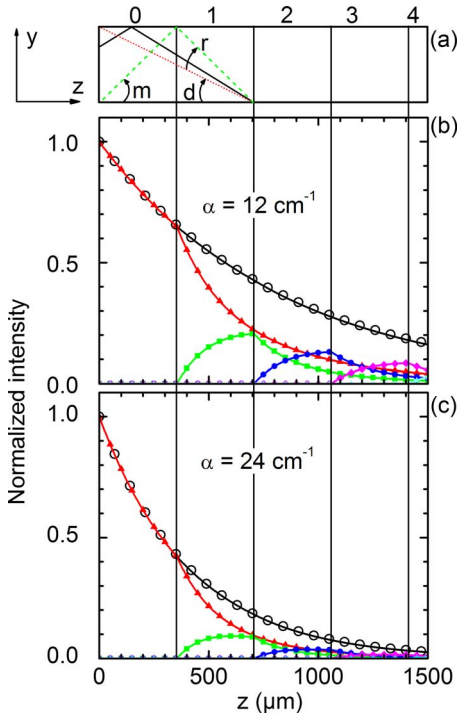

FIG. 3. (Color online) (a) Schematic sketch of a 2D longitudinal ray-tracing model. The numbers 0–4 on the top of the figure denote device segments but also give the numbers of allowed reflections. The angular range for direct light is *d*, *r* is for one reflection, and *m* is the maximum angle for which rays are allowed to leave the cavity. Three rays start from a source placed at the border between sections 1 and 2, giving the extreme cases of no (dotted red line) and one reflection (dashed green line) and one ray in between (solid black line). [(b) and (c)] Thermal IR light intensity leaving the front facet normalized to the allowed exit cone of the model outlined in (a). The intensity is plotted vs the *z* position of point sources placed at the bottom of the cavity separately according to the number of reflections that the rays experience. The attenuation due to absorption with α equal to (b) 12 cm^{-1} and (c) 24 cm^{-1} and due to the refractive-index jump at the semiconductor-air interface (Fresnel formulas for unpolarized IR light). Red triangles, green squares, blue dots, magenta rhombi, and cyan stars represent light that experienced no, one, two, three, and four reflections at the top or bottom. The solid black line represents their sum and the black opened circles represent the simple exponential decay according to α.

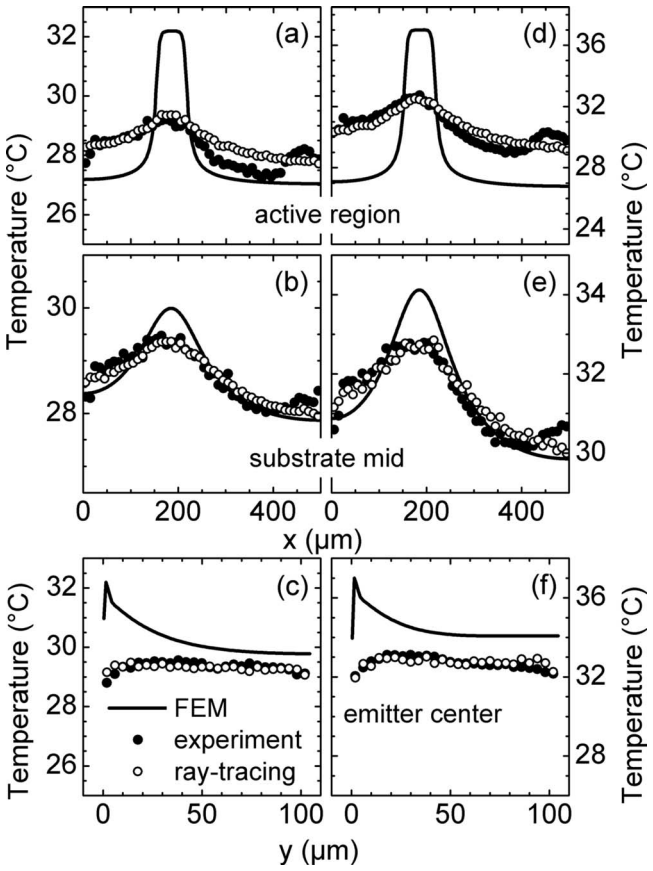

FIG. 4. Absolute temperature profiles from a QD laser operated at [(a)–(c)] 0.9 A and at [(d)–(f)] 1.8 A obtained as cuts from maps such as given in Figs. 1(b)–1(d). Solid lines represent the FEM results, closed circles are the MT results, and the open circles are the results from ray-tracing simulation using the FEM temperature maps: [(a) and (d)] lateral profiles around the active region; [(b) and (e)] lateral profiles around half the device height; [(c) and (f)] vertical profiles at the stripe center. All profiles are averaged from three pixel rows or columns for noise reduction.

Concluding this section, we stress that the detected image of a heat distribution from the laser diode is subject to propagation of thermal IR light inside the semitransparent GaAs substrate with two almost fixed parameters, a refractive index of $n=3.3$ (at a central wavelength of 5 μm) and a reflectivity of the top and bottom surfaces of $R=1$. The third parameter α which is governed by the substrate doping influences the shapes of the analyzed profiles to a larger extent.

B. Analysis of thermal images from devices

We start by applying the ray-tracing technique to the analysis of thermal image formation by using the QD lasers. Typical thermal maps as calculated by FEM, from MT experiments, and from our modeling approach (involving FEM and ray tracing) are shown in Figs. 1(b)–1(d), respectively. The *quantitative* comparison is based on cuts through these maps, which have been calibrated back to temperatures after ray tracing. In Fig. 4, original FEM data (lines), data from MT experiment (full circles), and FEM data after the above described processing (open circles) are compared for two operation currents of 0.9 A [Fig. 4(a)–4(c)] and 1.8 A [Fig. 4(d)–4(f)] in terms of lateral (along the active region and middle of the device) and vertical cuts (at the emitter center, along the growth direction). In all cases, there is very good agreement between the open and full circles. The only adjustment parameter in this comparison is, within extremely tight limits, the experimental heat-sink temperature. The FEM model assumes a fixed temperature of 25.0 °C at the device heat-sink interface, whereas in the experiment the heat-sink temperature was controlled to 25.0 ± 0.2 °C approximately 4 mm away, which could result in a small relative temperature difference. In order to nearly perfectly match model and experiment, heat-sink temperatures of 26.1 °C [0.9 A (Fig. 4)] and 25.0 °C [1.8 A (Fig. 5)] are assumed. In turn, such close agreement strongly indicates not only that propagation of thermal radiation within the cavity is a key issue toward quantitative MT analysis on a *microscopic* scale but also that the 2D-FEM model is sufficient to reproduce the experimental results. As mentioned earlier, the broadening of the MT images caused by diffraction does not explain the observed broadening effect.

In the second example we analyze time-dependent thermal distributions of the QW device during pulsed operation.

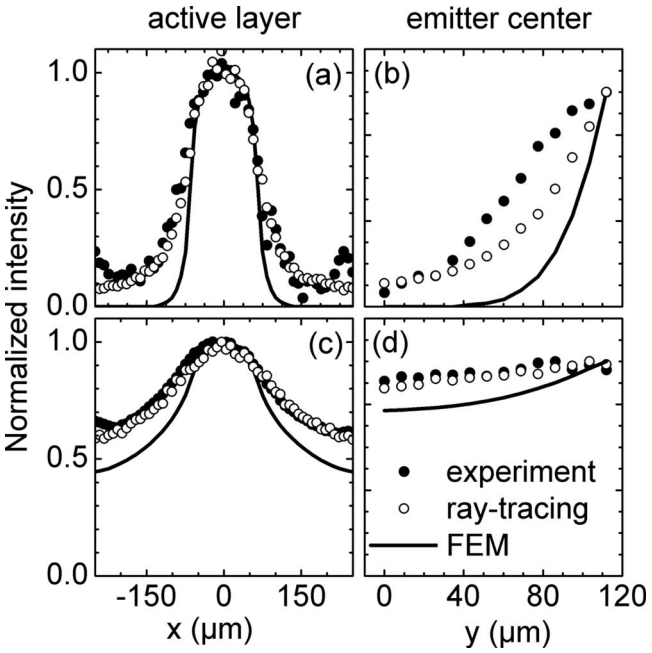

FIG. 5. Normalized temperature profiles from a QW laser operated at pulsed currents of 1 A. Solid lines represent the FEM results, open circles the ray-tracing results, and closed circles the results from MT: (a) lateral profiles at the active region and (b) vertical profiles at the emitter center from the transient thermal situation 15 μs after turn-on (synchronous lock-in MT with 100 μs long pulses, FEM simulation result taken at 15 μs after turn-on). (c) and (d) are analogous profiles after 11 ms (synchronous lock-in MT with 69 ms long pulses, FEM simulation at a point in time 11 ms after turn-on). For lateral cuts 2 rows (of 14 rows in total) and for vertical cuts 5 columns (of 58 in total) are averaged in the corresponding data matrices.

Since light propagation is instantaneous compared to the thermal turn-on dynamics in the device, ray tracing is able to predict its effect on the thermal image in the transient regime too. Analogous to the QD device, the quantitative comparison in Fig. 5 is based on cuts through thermal maps for a pulsed current of 1 A. Lateral profiles of the active region and vertical profiles of the emitter center for transient thermal situations 15 μs [Figs. 5(a) and 5(b)] and 11 ms [Figs. 5(c) and 5(d)] after turn-on are displayed. Note again the good agreement between MT images and the data calculated by subsequent FEM and ray-tracing modeling.

V. SUMMARY

We have analyzed the effect of propagation of thermal IR radiation within BA diode lasers onto thermal images of such devices. Ray-tracing of FEM-modeled temperature profiles and comparison with experimental MT data demonstrated that propagation of thermal IR light within the semitransparent semiconductor materials leads to substantially broadened images on a spatial scale of 10 μm. The main parameter that affects this broadening is the substrate doping which governs the absorption of the spreading IR light by free carriers. Consequently, for heavier doping identical temperature distributions will lead to narrower thermal images. The approach was confirmed by two applications, a QD laser and a QW laser. For QD lasers this is particularly important because for this type of laser devices the use of the emission wavelength as a thermal probe widely fails.

The concerted approach demonstrates that MT images recorded with spatial resolutions of better than ~10 μm contain information of the true bulk-temperature distribution of the operating laser device but modified by the propagating thermal radiation. In this way MT enables the verification of thermal simulations such as obtained by FEM for complete semiconductor laser devices without restriction to the active region only. This represents a novel and very useful experimental option. Thermography on a more macroscopic scale such as in the case of extended laser arrays,[19] where the achievable spatial resolution sets a more rigid limitation, or in cases where cross calibration with thermal wavelength shift is possible[8] is not affected by our findings.

ACKNOWLEDGMENTS

This study was funded by the European Commission within the project WWW.BRIGHTER.EU, under Contract No. IST-2005-035266. The QW devices have been produced within the German BMBF project BRILASI, under Contract No. 13N8601, and placed at our disposal by Götz Erbert and Frank Bugge of the Ferdinand-Braun-Institut für Höchstfrequenztechnik Berlin.

[1] V. K. Malyutenko, Proc. SPIE **4648**, 43 (2002).
[2] B. L. Meadows, F. Amzajerdian, N. R. Baker, V. Sudesh, U. N. Singh, and M. J. Kavaya, Proc. SPIE **5336**, 203 (2004).
[3] The camera microscope with sixfold magnification results in a resolution of 4 μm/pixel for full frame images of 384×288 pixels for a THERMOSENSORIK CMT 384M system. The actual, experimentally determined one amounts to about 6 μm with the spectral detection band confined to 3.5–6.0 μm wavelength.
[4] M. Kuball, S. Rajasingam, A. Sarua, M. J. Uren, T. Martin, B. T. Hughes, K. P. Hilton, and R. S. Balmer, Appl. Phys. Lett. **82**, 124 (2003).
[5] M. Ziegler, J. W. Tomm, T. Elsaesser, C. Monte, J. Hollandt, H. Kissel, and J. Biesenbach, J. Appl. Phys. **103**, 104508 (2008).
[6] F. Bugge, A. Knauer, S. Gramlich, I. Rechenberg, G. Beister, J. Sebastian, H. Wenzel, G. Erbert, and M. Weyers, J. Electron. Mater. **29**, 57 (2000).
[7] M. Ziegler, J. W. Tomm, T. Elsaesser, G. Erbert, F. Bugge, W. Nakwaski, and R. P. Sarzała, Appl. Phys. Lett. **92**, 103513 (2008).
[8] M. Ziegler, F. Weik, J. W. Tomm, T. Elsaesser, W. Nakwaski, R. P. Sarzała, D. Lorenzen, J. Meusel, and A. Kozlowska, Appl. Phys. Lett. **89**, 263506 (2006).
[9] O. C. Zienkiewicz and R. L. Taylor, *The Finite Element Method* (Butterworth-Heinemann, Oxford, UK, 2000).
[10] J. Mukherjee and J. McInerney, IEEE J. Sel. Top. Quantum Electron. **13**, 1180 (2007).
[11] W. Nakwaski, Int. J. Optoelectron. **5**, 451 (1990).
[12] R. P. Sarzała and W. Nakwaski, J. Therm. Anal. **36**, 1171 (1990).
[13] R. P. Sarzała and W. Nakwaski, Opt. Quantum Electron. **26**, 87 (1994).
[14] W. Nakwaski, J. Appl. Phys. **64**, 159 (1988).
[15] The homepage of the softwre vendor is www.zemax.com.
[16] We choose the temperature distribution of the QW-laser structure at 100 μs after turn-on because it shows a rather narrow temperature profile along the active region compared to the steady-state one. The original temperature profile is given by the solid black line in Fig. 2(a). This choice is particularly suitable for studying the effect of thermal radiation spreading.
[17] T. Skauli, P. S. Kuo, K. L. Vodopyanov, T. J. Pinguet, O. Levi, L. A. Eyres, J. S. Harris, and M. M. Fejer, J. Appl. Phys. **94**, 6447 (2003).
[18] 112 μm of the totally 115 μm high device correspond to semiconductor materials.
[19] A. Kozlowska, M. Latoszek, J. W. Tomm, F. Weik, T. Elsaesser, M. Zbroszczyk, M. Bugajski, B. Spellenberg, and M. Bassler, Appl. Phys. Lett. **86**, 203503 (2005).